

Exchange biasing of single-domain Ni nanoparticles spontaneously grown in an antiferromagnetic MnO matrix

Daniel P. Shoemaker,* Madeleine Grossman, and Ram Seshadri

*Materials Department and Materials Research Laboratory
University of California, Santa Barbara, CA, 93106, USA*

(Dated: November 3, 2018)

Exchange biased composites of ferromagnetic single-domain Ni nanoparticles embedded within large grains of MnO have been prepared by reduction of $\text{Ni}_x\text{Mn}_{1-x}\text{O}_4$ phases in flowing hydrogen. The Ni precipitates are 15-30 nm in extent, and the majority are completely encased within the MnO matrix. The manner in which the Ni nanoparticles are spontaneously formed imparts a high ferromagnetic–antiferromagnetic interface/volume ratio, which results in substantial exchange bias effects. Exchange bias fields of up to 100 Oe are observed, in cases where the starting Ni content x in the precursor $\text{Ni}_x\text{Mn}_{1-x}\text{O}_4$ phase is small. For particles of approximately the same size, the exchange bias leads to significant hardening of the magnetization, with the coercive field scaling nearly linearly with the exchange bias field.

I. INTRODUCTION

Exchange anisotropy, or exchange bias, is an interfacial phenomenon between ferromagnetic and antiferromagnetic domains which results in the shifting and broadening of magnetic hysteresis loops. Exchange bias is believed to result from the interaction of ferromagnetic (FM) spins with uncompensated antiferromagnetic (AFM) spins at the FM/AFM interface.^{1,2,3} Since its discovery in partially oxidized Co/CoO nanoparticles by Meiklejohn and Bean,⁴ exchange bias has been observed and engineered in core-shell nanoparticles,⁵ thin films,⁶ and granular composites.⁷ These architectures are utilized because a high proportion of FM spins must be interfacial in order for the AFM switching behavior to appreciably affect the FM coercivity. While they achieve a high interface/volume ratio, core-shell nanoparticles and thin film architectures do not result in large quantities of exchange-biased material. As an alternative, novel methods of processing exchange biased systems have been explored, including coevaporation,⁸ mechanical milling,⁹ and spontaneous phase separation.¹⁰

Initial reports from Sort *et al.*¹¹ have demonstrated hydrogen reduction of $\text{Fe}_{0.2}\text{Cr}_{1.8}\text{O}_3$ to produce metal/oxide composites. Different transition metals reduce sequentially, resulting in nanosized Fe particles within micron sized Cr_2O_3 grains. Interaction between the ~ 10 nm Fe precipitates and the bulk Cr_2O_3 provides exchange bias shifts of 10 Oe. Reduction kinetics of the system CoCr_2O_4 – Co_3O_4 have been reported by Bracconi and Dufour¹², and Kumar and Mandal¹³ have produced Co/ Cr_2O_3 composites directly from nitrate precursors. Recently, Toberer *et al.*¹⁴ have demonstrated that remarkable microstructures with aligned porosity can be observed when the reduction product shares a common oxygen sublattice with the precursor.

Here we report on hydrogen reduction of the system $\text{Ni}_x\text{Mn}_{3-x}\text{O}_4$ to form Ni/MnO composites with striking microstructures associated with substantial exchange biasing. The Ni particles exhibit bulk saturation magne-

tization values, and exchange bias is observed below the Néel temperature of MnO at $T_N = 119$ K. Surface and interior particle size analysis reveals that this system produces Ni nanoparticles on the order of 15 nm to 30 nm. Size-dependent exchange bias phenomena are manifested in trends between the Ni content of the precursor spinel and the exchange and coercive fields of the reduced composite.

II. EXPERIMENTAL

Single-phase ceramic monoliths were prepared by solid-state reactions of oxalates, similar to that of Wickham.¹⁵ Oxalates are versatile precursors for mixed metal oxides, and have found extensive use in recent years to produce substituted binary^{16,17} and ternary^{14,18,19} compounds.

Stoichiometric amounts of nickel acetate and manganese acetate [$\text{Ni}(\text{CH}_2\text{COOH})_2 \cdot 4\text{H}_2\text{O}$ and $\text{Mn}(\text{CH}_2\text{COOH})_2 \cdot 4\text{H}_2\text{O}$, Aldrich 99%] were added to a solution containing one equivalent of glacial acetic acid. Excess oxalic acid monohydrate [$\text{H}_2(\text{C}_2\text{O}_4) \cdot \text{H}_2\text{O}$, Fisher 99.9%] was mixed in a separate solution and both were stirred at 90°C. Addition of the oxalic acid to the dissolved acetates results in coprecipitation of very fine, single-phase nickel-manganese oxalates in which the metals are mixed on the atomic scale. The oxalate powders, $\text{Ni}_x\text{Mn}_{3-x}(\text{C}_2\text{O}_4)_3 \cdot 2\text{H}_2\text{O}$, were washed with deionized water and dried at 90°C, calcined in alumina boats in air at temperatures ranging from 780° to 1200°C for 10 h, then quenched into water to prevent conversion to α - Mn_2O_3 or to NiMnO_3 . The resulting single-phase $\text{Ni}_x\text{Mn}_{3-x}\text{O}_4$ spinel powder was pressed into pellets at 100 MPa and sintered at 1325°C for 24 h, then annealed at the previous calcination temperature and water quenched.

Reductions were performed in alumina boats in a tube furnace under 5% H_2/N_2 with a flow rate of approximately 30 sccm. Once the gas mixture had equilibrated, the specimens, as pellets, were heated at 2°C/min to 650°C, 700°C, or 725°C, held for 2 h, then cooled at

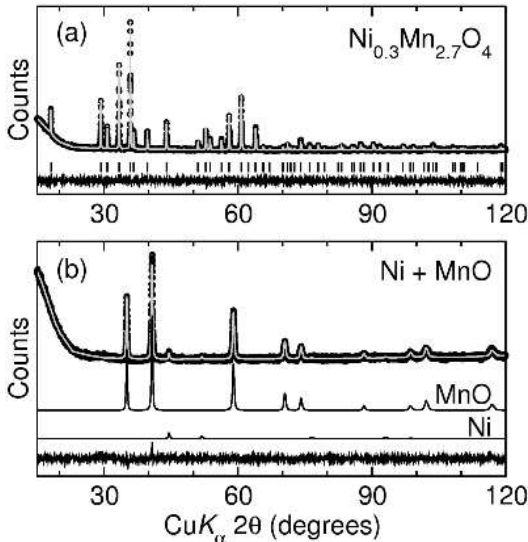


FIG. 1: X-ray diffraction Rietveld refinements of (a) $\text{Ni}_{0.3}\text{Mn}_{2.7}\text{O}_4$ single-phase tetragonal spinel (hausmannite) precursor, and (b) the *fcc*-Ni/rock-salt MnO composite produced by reduction of the above spinel in 5% H_2/N_2 .

$10^\circ\text{C}/\text{min}$ to room temperature. Reduced samples were verified to be Ni/MnO by x-ray diffraction (XRD, Philips X'Pert with CuK_α radiation) and Rietveld refinement using the XND code.²⁰ Composites were characterized by thermogravimetric analysis (TGA, Cahn TG-2141), scanning electron microscopy (SEM, FEI Sirion XL40), focused ion beam milling and microscopy (FIB, FEI DB235), and SQUID magnetometry (Quantum Design MPMS 5XL).

III. RESULTS AND DISCUSSION

The calcining of the single-phase Ni/Mn oxalates, according to the phase diagram presented by Wickham,¹⁵ results in single phase spinel-related compounds that are not all cubic. Wickham¹⁵ has reported that in their high-temperature state, bulk samples of $\text{Ni}_x\text{Mn}_{3-x}\text{O}_4$ with x between 0.15 and 1.00 are cubic spinels before decomposing into NiMnO_3 and $\alpha\text{-Mn}_2\text{O}_3$ in the temperature range of 705° to 1000°C . Upon water quenching, samples prepared with $x < 1$ and fired at $\geq 1000^\circ\text{C}$ are observed to distort from the high-temperature cubic spinel reported by Wickham into single-phase hausmannite-type tetragonal spinels in space group $I4_1/amd$. Slow-cooling, air-quenching, or quenching in flowing nitrogen are insufficient to prevent decomposition of the solid solution.

Rietveld refinement of the room-temperature XRD pattern for the water-quenched compound $\text{Ni}_{0.30}\text{Mn}_{2.7}\text{O}_4$ is shown in Fig. 1(a). Only peaks for the hausmannite-type solid solution are evident; this is a requirement for the final reduced composite to be homogeneous in terms of the distribution of Ni precipitates. The refinement assumes a “normal” spinel, where Ni^{2+} and Mn^{2+} occupy

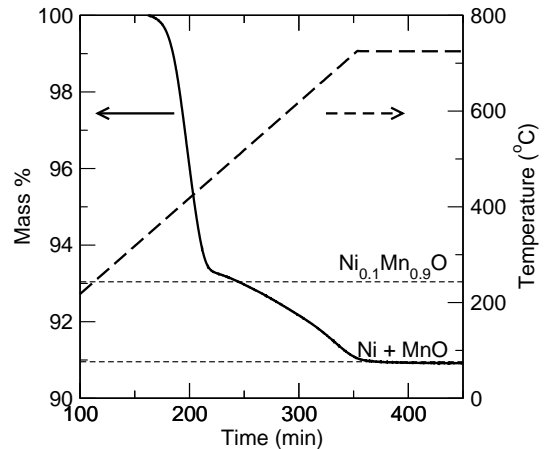


FIG. 2: TGA of a $\text{Ni}_{0.3}\text{Mn}_{2.7}\text{O}_4$ sample shows that reduction proceeds by an initial reaction to rocksalt $\text{Ni}_{0.1}\text{Mn}_{0.9}\text{O}$ solid solution, followed by a reduction of Ni^{2+} into metallic Ni.

the 4b tetrahedral sites. Mn^{3+} in the 8c octahedral sites causes a cooperative Jahn-Teller distortion which leads to a loss of cubic symmetry.²¹ An accurate determination of the cation distribution may be obtained by neutron diffraction and has been investigated by Larson *et al.*²² When sintered at 1325°C , samples with x near 1 partially decompose into mixtures of NiO and $\text{Ni}_{1-\delta}\text{Mn}_{2+\delta}\text{O}_4$ as described by Wickham,¹⁵ but subsequent annealing at 800°C for 72 h ensures the formation of a single-phase tetragonal spinel. Dense pellets and micron-sized powder are both suitable precursors for hydrogen reduction because the dimensions of the precipitates and pores are orders of magnitude smaller than the grain size in either case. Adequately high oxygen mobility at the reduction temperature allows the reaction to permeate the sample regardless of any lack of preexisting porosity.

In all cases, TGA analysis confirms the total amount of nickel precipitated (and thus the stoichiometry of the precursor spinel) during hydrogen reduction. A TGA weight loss curve for $\text{Ni}_{0.3}\text{Mn}_{2.7}\text{O}_4$ is shown in Fig. 2. The weight loss curve reveals that the single-phase spinel first reduces to a rocksalt ($\text{Ni}_{0.1}\text{Mn}_{0.9}\text{O}$) solid solution, followed by precipitation of metallic Ni. This progression is verified by the fact that incompletely reduced samples display an MnO lattice parameter that is smaller than the theoretical value, due to Ni substitution. X-ray diffraction Rietveld refinement of the final composite product obtained after reduction in 5% H_2/N_2 indicate only rock-salt MnO and face-centered cubic Ni [Fig. 1(b)].

High-spin Mn^{2+} in octahedral coordination has an ionic radius of 0.83 \AA in contrast to octahedral Ni^{2+} which has a radius of only 0.69 \AA .²³ Consequently, when Ni^{2+} enters product MnO lattice, there is significant shrinkage of the cell parameter, which can be used to estimate the degree of conversion of the starting phases into pure Ni/MnO. The MnO lattice parameter obtained from Rietveld refinement is plotted in Fig. 3(a) as a function of the Ni content in the single-phase hausmannite/spinel

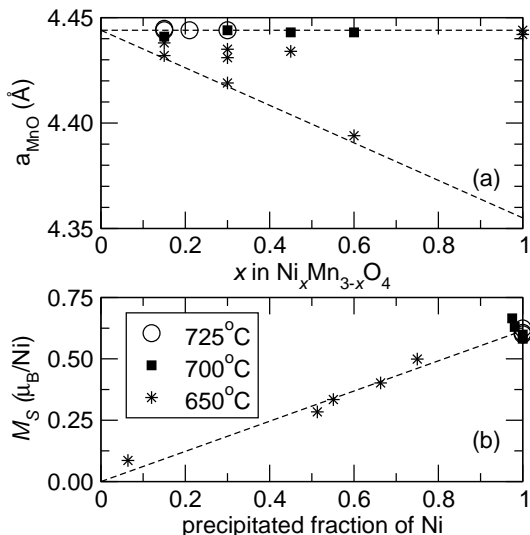


FIG. 3: (a) Lattice parameter of MnO obtained by Rietveld refinement of samples after hydrogen reduction at varying temperatures. The diagonal dotted line is the calculated lattice parameter of a (Ni,Mn)O solid solution, while the top line represents the desired conversion to pure MnO. (b) Magnetic saturation of reduced Ni/MnO samples increases linearly with the completeness of Ni reduction as determined by a_{MnO} from XRD. All magnetic data concerning coercivity or exchange bias was measured from samples with complete Ni reduction and thus $M_S \approx 0.6\mu_B/\text{Ni}$.

precursor. The cell parameter of pure MnO, 4.444 Å is also indicated as a horizontal dashed line. It is seen that for small substitution of Ni (x in the starting phases) the reduction temperature must be increased from 650°C to 725°C to ensure complete reduction and avoid the rock-salt (Ni,Mn)O solid solution. Depression of the required reduction temperature of $\text{Ni}_x\text{Mn}_{3-x}\text{O}_4$ as x deviates from Mn_3O_4 is a consequence of the higher ionization energy of Ni^{2+} . In other words, more energy is released by reduction of Ni^{2+} ions than of Mn^{2+} , so the reduction to metal occurs more readily when x is larger. The greater ease of reduction of Ni over Mn is suggested by the appropriate Ellingham diagram.²⁴ The saturation magnetization M_S of the magnetic Ni nanoparticle precipitates can be used in tandem with the values of a_{MnO} obtained from Rietveld refinement to determine the completeness of Ni reduction. This is shown in Fig. 3(b), where agreement is seen between the convergence of a_{MnO} and M_S to their respective theoretical values of 4.444 Å and $0.6\mu_B/\text{Ni}$ for a completely reduced $x\text{Ni}/\text{MnO}$ composite, regardless of x .

Hydrogen reduction of single-phase oxide monoliths can lead to striking hierarchically porous microstructures, which have been characterized by Toberer *et al.*^{14,19,25} At first glance, low-magnification SEM micrographs of $\text{Ni}_x\text{Mn}_{3-x}\text{O}_4$ precursor spinels and Ni/MnO reduced samples [Fig. 4(a) and Fig. 4(b), respectively] appear nearly identical. However, higher magnifica-

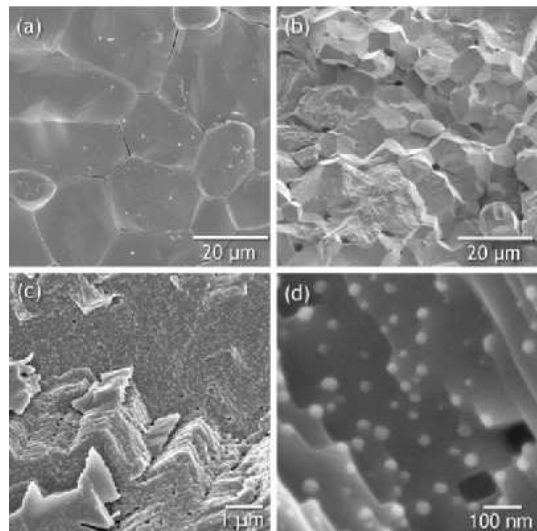


FIG. 4: Representative scanning electron microscope images: (a) The as-sintered surface of a dense pellet of $\text{Ni}_x\text{Mn}_{3-x}\text{O}_4$ with $x = 0.3$. (b) The fracture surface of the material obtained from reducing the sample in (a) at 725°C for 2 h. (c) and (d) are the sample in (b) shown at higher magnification. The highly porous and crystalline matrix of MnO is seen in (c), and at higher magnification, small Ni particles with sizes in the 30 nm to 40 nm range are seen as bright objects on a darker background.

tion [Fig. 4(c) and (d)] reveals that reduced composites contain aligned pores in rock-salt MnO covered with Ni metal nanoprecipitates. It has been previously suggested^{14,25} that the shared oxide sublattice of spinel and rocksalt allows the transformation from one to the other to take place without reconstruction. Porosity is introduced during the spinel to rocksalt transformation while leaving the oxygen framework largely intact. The associated volume loss gives rise to a pore structure that can be regarded as negative crystals – voids in crystals that possess the same facets as the crystals themselves do.

Although the pores are as small as 20 nm, the pore and surface edges are aligned at right angles over the entire breadth of the 20 μm grains. This long-range alignment implies that the MnO grains are in fact single crystals with the same orientation and extent as the pre-reduction spinel grains.^{14,19} Increasing the reduction temperatures should lead to densification and closing of the pores in the MnO monolith. However, in the interest of maintaining small Ni nanoparticles (and thus a high interface/volume ratio), and because the majority of nanoparticles are completely encased in MnO even in porous samples, reduction was performed at the lowest temperature that allowed complete Ni precipitation.

If we assume that for the different values of x , the number of nuclei are the same, and that increasing x only affects the growth (*ie.* the diameter) of the particles, then we would expect only a weak dependence (changing as $x^{1/3}$) of the particle diameter rate on x . If

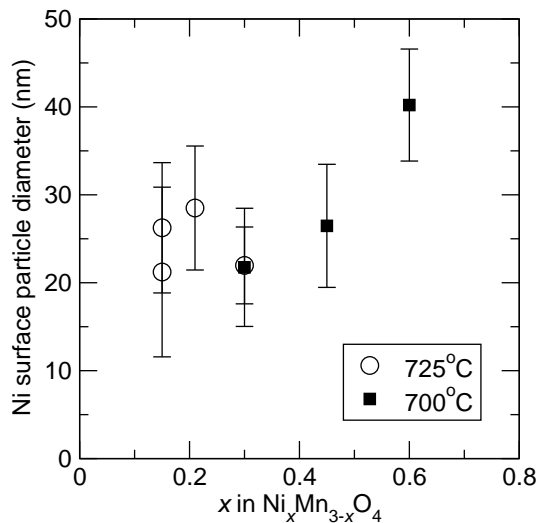


FIG. 5: The mean diameters of the Ni particles on the surface of the MnO matrix as a function of the initial Ni content x in $\text{Ni}_x\text{Mn}_{3-x}\text{O}_4$. Error bars indicate one standard deviation in the particle diameter. Typically at least 30 distinct particles were counted in preparing the distributions. It is seen that most in most samples, the sizes are somewhat independent of x and are clustered around 30 nm.

we assume that increasing x also increases the number of Ni nuclei upon reduction, then average particle diameter would show an even weaker dependence on x . We have analyzed the Ni particles in the SEM images of the surfaces of the monoliths by using the program IMAGEJ²⁶ to prepare histograms of particle size distributions. These are plotted in Fig. 5 for the different monoliths. It is seen that mean particle diameters range from ~ 15 nm to 35 nm, but there is no clear trend in size, at least until a nickel content of $x = 0.60$ is reached.

Indeed, in the different monoliths, a clearer correlation is found for Ni particle size with the specific crystallographic face of MnO upon which it grows, rather than the starting x value. It is evident in Fig. 6(a) that for a $x = 0.45$ specimen, regions can be found which exhibit a wide variety of surface particle sizes and spacings depending on the nucleation environment. The coherent pore structure introduced by reduction produces square or triangular facets seen in Fig. 6(a) which correspond to exposed $\{100\}$ or $\{111\}$ faces.

Cross-sections of reduced grains produced by FIB milling, shown in Fig. 6, reveal that the bulk MnO contains Ni nanoparticles of similar dimensions as those on the surface. Porosity is still prevalent in the bulk of the monoliths as it is in the images of the monolith surface. This is necessary to accommodate the volume loss of the structure while retaining the size and alignment of the MnO grains. By a comparison of lattice parameters, and assuming no sintering during reduction, the fraction of intragranular porosity produced by the conversion of $\text{Ni}_x\text{Mn}_{3-x}\text{O}_4$ to $x\text{Ni}/\text{MnO}$ increases linearly from 16% when $x = 0$ to 39% when $x = 0.6$, which is in rough agree-

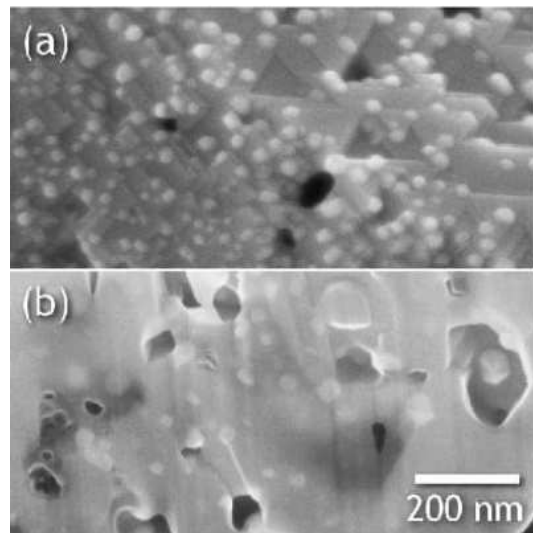


FIG. 6: (a) Fracture surface of a reduced sample (700°C, 2 h) of $\text{Ni}_x\text{Mn}_{3-x}\text{O}_4$ with $x = 0.45$, and (b) the surface of a FIB-cut sample of the product formed on reduction (700°C, 2 h) of $\text{Ni}_x\text{Mn}_{3-x}\text{O}_4$ with $x = 0.60$. The two images are displayed at the same magnification. It is seen in (a) that different faces of the underlying MnO seem to nucleate different particle sizes of *fcc*-Ni. In (b), it is seen that the Ni particles are found within the MnO matrix as well, and not simply on the surface.

ment with observations of the intragranular pore volume in FIB-milled samples. Most Ni nanoparticles observed in cross-section [Fig. 6(b)] are completely encased within the MnO matrix. Based upon the observed surface density of Ni particles and assuming 100 nm diameter pores, it can be determined that the observed surface Ni particles only constitute about 20% of the volume of Ni that must be precipitated. Therefore, we estimate that approximately 80% of the Ni grains are encased within the MnO matrix.

Magnetic hysteresis loops for an $x = 0.3$ sample (Fig. 7) display at 5 K, a loop shift H_E characteristic of exchange biased systems. Above the Néel temperature of MnO, $T_N = 119$ K, the hysteresis loop is centered about $H = 0$. After field cooling at $H = 50$ kOe, the coercive field is broadened and shifted $H_E = 100$ Oe in opposition of the cooling field direction. The exchange behavior can be influenced by many factors, including Ni particle size, the amount and orientation of the FM-AFM interface, temperature, and the cooling field.³ We anticipate that in the size regime studied here (near 20 nm) the Ni nanoparticles are single-domain magnets and that the coercivity below the blocking temperature should not show a strong size-dependence.²⁷ Fig. 8(a) shows that as the nickel content x increases, H_C decreases for samples reduced at either 700°C or 725°C. At both reduction temperatures, the highest H_C is found for the smallest x , and the smallest H_C is found for the largest x .

Additionally, the decrease in H_C for $x = 0.3$ samples reduced at 725°C as opposed to 700°C implies increased

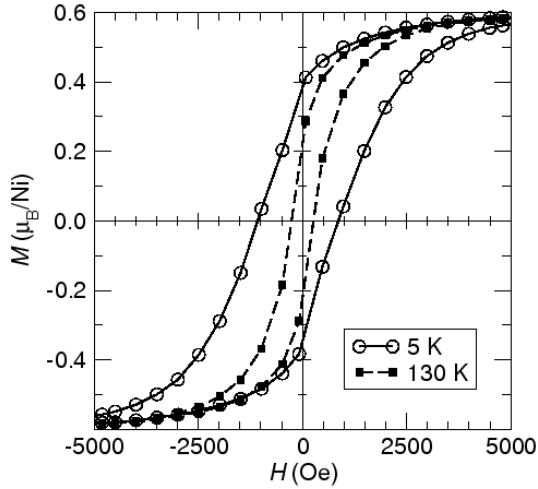


FIG. 7: Magnetization M as a function of magnetic field H for an Ni/MnO composite with $x = 0.3$ above T_N (dashed) and field-cooled under a 50 KOe field to 5 K (solid). Exchange bias leads to a broadening (associated with the coercivity H_C) and shift (associated with the exchange field H_E) of the field-cooled loop at 5 K.

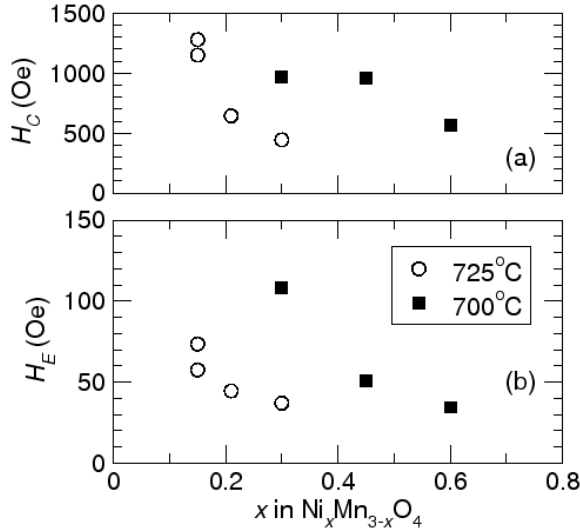


FIG. 8: (a) Coercive field H_C and (b) Exchange-bias field H_E as a function of the initial Ni content x in the reduced Ni/MnO composites. The coercivity H_C of the Ni nanoparticles decreases with Ni content for each firing temperature in response to the increased fraction of interfacial spins as Ni content is decreased. Exchange bias effects become less pronounced as well, with increasing Ni content in the oxide precursor.

coalescence of Ni particles as the temperature increases. We therefore anticipate that the increased coercivity as size is decreased arises from the same interfacial coupling that results in the increased exchange bias.

In exchange biased nanostructures of spherical FM particles in an AFM matrix, the strength of the exchange field H_E has been suggested to vary as

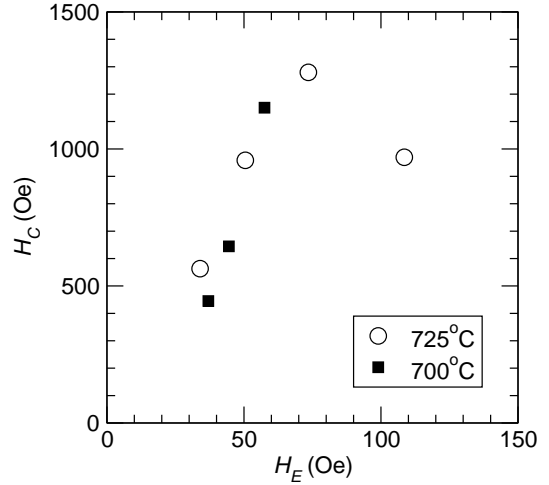


FIG. 9: Coercive field as a function of exchange field at 5 K for the different Ni/MnO composites. For most of the composite systems, H_C varies nearly linearly with H_E .

$$H_E = \frac{6E_A}{M_S d_{\text{FM}}}$$

where E_A is the interfacial coupling energy per unit area, M_S is the saturation magnetization of the FM, and d_{FM} is the diameter of the FM particle.⁷ Assuming this model to be correct, we anticipate that the exchange field H_E should decrease with increasing ferromagnetic particle size. If, with increasing x in our systems, Ni particle size indeed increases, then our results are broadly consistent with this model.

In Fig. 9 we plot the 5 K coercivity as a function of the exchange field for the different systems measured, data for which are displayed in Fig. 8. We see that the coercivity varies nearly linearly with the exchange field, with the exception of one outlier. Gökemeijer *et al.*²⁸ have recently measured biasing of ferromagnets on different CoO surfaces and have concluded that on the uncompensated CoO surfaces, exchange biasing, and the associated shift of hysteresis is found, but on compensated CoO surfaces, the effect of the interface is simply to increase coercivity. The magnetic structure of MnO is not simple²⁹ and the architectures described here of nearly spherical ferromagnetic particles embedded in an antiferromagnetic host cannot be described in terms of simple interfaces. Given this, we suggest that perhaps both effects, of the uncompensated as well as the compensated surfaces are playing a role, and the linear relation between coercivity and exchange is simply an indication of increasing interfacial area between the two magnetic components.

IV. CONCLUSIONS

We have demonstrated that hydrogen reduction of $\text{Ni}_x\text{Mn}_{3-x}\text{O}_4$ spinels produces Ni/MnO composites with

significant interfacial area between antiferromagnetic MnO and ferromagnetic Ni, and associated exchange bias. With increasing nickel content x , these effects decrease, presumably because of a decrease in the relative proportion of interfacial spins in the ferromagnet. Exchange bias effects at the FM–AFM interface lead to an increase in H_C with decreasing Ni content, along with a $1/x$ dependence of H_E . A nearly linear relationship is found between H_C and H_E in these systems.

V. ACKNOWLEDGMENTS

This work was supported by the donors of the American Chemical Society Petroleum Research Fund, and the National Science Foundation through a Career Award (DMR 0449354) to RS, and for the use of MRSEC facilities (DMR 0520415). MG was supported by a RISE undergraduate fellowship.

-
- * Electronic address: dshoe@mrl.ucsb.edu
- ¹ M. Blamire and B. Hickey, *Nature Mater.* **5**, 87 (2006).
 - ² W. Kuch, L. I. Chelaru, F. Offi, J. Wang, M. Kotsugi, and J. Kirschner, *Nature Mater.* **5**, 128 (2006).
 - ³ J. Nogués and I. K. Schuller, *J. Magn. Magn. Mater.* **192**, 203 (1999).
 - ⁴ W. H. Meiklejohn and C. P. Bean, *Phys. Rev.* **105**, 904 (1957).
 - ⁵ V. Skumryev, S. Stoyanov, Y. Zhang, G. Hadjipanayis, D. Givord, and J. Nogués, *Nature (London)* **423**, 850 (2003).
 - ⁶ M. R. Fitzsimmons, S. D. Bader, J. A. Borchers, G. P. Felcher, J. K. Furdyna, A. Hoffmann, J. B. Kortright, I. K. Schuller, T. C. Schulthess, S. K. Sinha, et al., *J. Magn. Magn. Mater.* **271**, 103 (2004).
 - ⁷ J. Nogués, J. Sort, V. Langlais, V. Skumryev, S. S. nach, J. S. M. noz, and M. D. Baró, *Phys. Rep.* **422**, 65 (2005).
 - ⁸ J.-Y. Yi, G. A. Hirata, and M. L. Rudee, *Mater. Res. Soc. Symposia Proceedings* **674**, T3.4.1 (2001).
 - ⁹ J. Sort, J. Nogués, X. Amils, S. S. nach, J. S. M. noz, and M. D. Baró, *Appl. Phys. Lett.* **75**, 3177 (1999).
 - ¹⁰ K. Narita, S. Koga, and Y. Motowaki, *J. Appl. Phys.* **52**, 5751 (1981).
 - ¹¹ J. Sort, V. Langlais, S. Doppiu, B. Dieny, S. Suriñach, J. S. M. noz, M. D. Baró, C. Laurent, and J. Nogués, *Nanotechnol.* **15**, S211 (2004).
 - ¹² P. Bracconi and L. C. Dufour, *J. Phy. Chem.* **79**, 2400 (1975).
 - ¹³ P. Anil Kumar and K. Mandal, *J. Appl. Phys.* **101**, 113906 (pages 5) (2007).
 - ¹⁴ E. S. Toberer and R. Seshadri, *Adv. Mater.* **17**, 2244 (2005).
 - ¹⁵ D. G. Wickham, *J. Inorg. Nucl. Chem.* **26**, 1369 (1964).
 - ¹⁶ A. S. Risbud, N. A. Spaldin, Z. Q. Chen, S. Stemmer, and R. Seshadri, *Phys. Rev. B* **68**, 205202 (2003).
 - ¹⁷ G. Lawes, A. S. Risbud, A. P. Ramirez, and R. Seshadri, *Phys. Rev. B* **71**, 045201 (2005).
 - ¹⁸ E. Toberer, A. Joshi, and R. Seshadri, *Chem. Mater.* **17**, 2142 (2005).
 - ¹⁹ E. S. Toberer, J. P. Lofvander, and R. Seshadri, *Chem. Mater.* **18**, 1047 (2006).
 - ²⁰ J. Bézar and G. Baldinozzi, *IUCr-CPD Newsletter* **20**, 3 (1998).
 - ²¹ J. B. Goodenough, *Ann. Rev. Mater. Sci.* **28**, 1 (1998).
 - ²² E. G. Larson, R. J. Arnott, and D. G. Wickham, *J. Phys. Chem. Solids* **23**, 1771 (1962).
 - ²³ R. D. Shannon, *Acta Crystallogr. A* **32**, 751 (1976).
 - ²⁴ W. W. Smeltzer and D. J. Young, *Prog. Solid State Chem.* **10**, 17 (1975).
 - ²⁵ E. Toberer, M. Grossman, T. Schladt, F. Lange, and R. Seshadri, *Chem. Mater.* **19**, 4833 (2007).
 - ²⁶ W. S. Rasband, *Imagej* (1997–2007), URL <http://rsb.info.nih.gov/ij/>.
 - ²⁷ B. D. Cullity, *Introduction to Magnetic Materials* (Addison-Wesley, Reading, 1972).
 - ²⁸ N. J. Gökemeijer, R. L. Penn, D. R. Veblen, and C. L. Chien, *Phys. Rev. B* **63**, 174422 (2001).
 - ²⁹ A. L. Goodwin, M. G. Tucker, M. T. Dove, and D. A. Keen, *Phys. Rev. Lett.* **96**, 047209 (pages 4) (2006).